Aboveground compressed air energy storage systems: Experimental and numerical approach

Emeric Dormoy [a,b], Brice Le Lostec [b], Didier Haillot [a,*]

[a] *École de Technologie Supérieure, Mechanical engineering department, Montréal, Canada*
[b] *Laboratory of Energy Technologies, Hydro-Québec Research Institute, Shawinigan, Québec, Canada*

ARTICLE INFO

ABSTRACT

The transition towards renewable energy sources necessitates reliable energy storage solutions to address the intermittency of solar and wind power. Among these solutions, compressed air energy storage technology holds promise, particularly in aboveground installations. While underground compressed air energy storage systems have shown potential at the grid scale, the focus on smaller aboveground installations is increasing due to their flexibility and higher energy density, yet they remain less mature and require further investigation. This research presents a comprehensive analysis of an aboveground system using both experimental data and numerical simulations, develops numerical model with real air properties and employs a quasi-steady-state approach. Experimental data calibration ensured model accuracy with a mean absolute percentage error below 4.0%, and parametric analysis revealed significant variations in round-trip efficiency, notably improving from 4.5% to 16.0% by increasing turbine stages from one to three with preheating. Further analysis confirmed the feasibility and relevance of integrating thermal energy storage into the system, aligning with the adiabatic concept, where compression heat is stored for subsequent expansion preheating, thereby enabling fully heated expansion using a three-stage turbine.

1. Introduction

Following COP28, nearly 200 parties committed to limiting global warming to 1.5 °C, necessitating a 43 % emission cut by 2030 relative to the 2019 level and achieving net zero by 2050 [1]. Key objectives include tripling global renewable energy capacity and transitioning away from fossil fuels. While the International Energy Agency (IEA) identifies the electricity and heat generation sector as a major contributor to greenhouse gas emissions [2], electricity demand is projected to increase by 80 % to more than 150 % by 2050, depending on specific scenarios [3], emphasizing the urgent need for a global energy transition. In the context of renewable energy development, a pivotal component of this transition, is, however, challenged by the intermittent nature of trending renewable energy sources such as solar and wind energy production, as both rely on specific weather conditions. Although the predictability of this intermittence allows for some planning, it introduces uncertainty and insecurity regarding anticipated energy production [4]. Non-intermittent energy sources such as biogas, biofuels, and hydroelectricity offer potential solutions to decarbonize electricity production. Nonetheless, biogas and biofuels continue to

release greenhouse gases during combustion. Hydroelectricity, while predictable and constant, requires specific geographic locations for new site construction and represent environmental issues [5]. Thus, the deployment of solar and wind technologies appears promising if the intermittence challenge is effectively addressed, particularly when complemented with non-intermittent energy sources.

Among the solutions proposed to mitigate the intermittency of renewable energy sources such as solar and wind, Electrical Energy Storage (EES) dedicated to the grid is often considered the most promising [6]. Beyond ensuring the stability of energy production from intermittent sources, EES can be utilized to manage peak periods [7]. EES technologies can store excess energy generated during periods of low demand and release it during high demand, thus stabilizing the grid and reducing reliance on fossil fuel-based peaking power plants. This not only enhances the efficiency of renewable energy systems but also contributes to reducing greenhouse gas emissions.

Several EES technologies are available, categorized according to the form of stored energy. The current literature extensively covers the state-of-the-art in EES, offering a comprehensive overview of both the technical and economic aspects of these technologies. Chen et al. [5] conducted an extensive review of various EES technologies, highlighting

* Corresponding author.
E-mail address: didier.haillot@etsmtl.ca (D. Haillot).

Nomenclature

Symbols

A	area (m^2)
c_p	specific heat capacity (J/kg.K)
$\dot{c}$	heat capacity flow rate (W/K)
E	Total energy (J)
H	enthalpy (J)
h	specific enthalpy (J/kg)
h_{conv}	heat convection coefficient (W/m^2.K)
K	global heat transfer coefficient (W/K.m^2)
ke	Kinetic energy (J)
$\dot{m}$	mass flow rate (kg/s)
N	number of stages
n	polytropic index
N_{275}	number of 275-liter reservoir
N_{320}	number of 320-liter reservoir
N_{sample}	sample size
P	pressure (Pa)
pe	Potential energy (J)
Q	transferred heat (J)
$\dot{Q}$	heat transfer rate (W)
T	temperature (K)
t	time (s)
U	internal energy (J)
V	volume (m^3)
v	specific volume (m^3/kg)
w	specific work (J/kg)
W	work (J)
$\dot{W}$	power (W)

Greek letters

β	compression/expansion ratio
γ	specific heat ratio
η	efficiency

Subscripts

amb	ambient
c	compression
e	expansion
el	electrical
he	heat exchanger
i	stage number identification
in	input
mec	mechanical
out	output
pol	polytropic
res	air reservoir
th	thermal
tot	total

Abbreviations

A-CAES	Adiabatic Compressed Air Energy Storage
CAES	Compressed Air Energy Storage
D-CAES	Diabatic Compressed Air Energy Storage
EES	Electrical Energy Storage
I-CAES	Isentropic Compressed Air Energy Storage
MAPE	Mean Absolute Percentage Error
RMSE	Root Mean Square Error
RTE	Round Trip Efficiency
TES	Thermal Energy Storage

their technical characteristics and applications. Luo et al. [7] focused on the role of CAES in large-scale power systems, particularly its integration with renewable energy sources, and presented an overview of multiscale CAES technologies, their economic characteristics, and the challenges associated with their future development. Zhang et al. [8] categorized ESS technologies into five major groups and analyzed their performance characteristics. This study also examined the application of these technologies in different segments of the power system and identified critical challenges and opportunities for their future development. Notably, Zakeri and Syri [9] have performed a meticulous technicoeconomic analysis of available EES technologies, emphasizing their life cycle costs.

To provide a clear comparison of various EES technologies, Table 1 presents a non-exhaustive summary of key metrics found primarily sourced from Zhang et al. [8], as it represents a recent and comprehensive contribution to the field. This table highlights the energy capacity, power rating, energy density, energy efficiency, lifetime, power capital cost, and energy capital cost for different EES technologies, including Pumped Hydro Storage (PHS), both underground and aboveground Compressed Air Energy Storage (CAES) and electrochemical systems like lithium-ion and lead-acid batteries. For aboveground CAES data, metrics were gathered from Bazdar et al. [10], who provided a comprehensive review of CAES systems, discussing their design criteria, integration potential, and recent technological advancements, while also addressing the limitations and future perspectives of CAES in various energy system applications.

From the data in Table 1, several key trends can be observed. Mechanical systems, such as PHS and underground CAES, exhibit significantly higher energy capacities and power ratings compared to electrochemical systems. For instance, PHS can achieve energy capacities ranging from 500 to 8000 MWh and power ratings from 100 to 5000 MW, making it suitable for large-scale applications. However, limited geographic availability and environmental impacts constrain its future deployment [4]. Underground CAES offers a promising alternative with similar benefits and broader site potential [11]. With energy capacities of 600–3000 MWh and power ratings of 5–300 MW, underground CAES utilize existing infrastructure such as depleted natural gas fields or salt caverns for storage, providing greater flexibility and

Table 1

Comparative metrics of various EES technologies based on [8,10].

EES	Mechanical			Electrochemical	
Characteristics	PHS [8]	UG CAES [8]	AG CAES [8,10]	Li-ion [8]	Lead-Acid [8]
Energy capacity (MWh)	500–8000	600–3000	<0.1 [10]	0–10	0–40
Power rating (MW)	100–5000	5–300	0–10 [10]	0–100	0–40
Energy density (Wh/L)	1–2	3–6	>6 [10]	200–500	50–90
Round trip efficiency (%)	70–85	<70	<70 [8]	90–97	75–85
Lifetime (year)	30–60	30–40	20–40 [10]	5–15	5–15
Power capital cost ($/kW)	2500–4600	400–800	500–1550 [10]	1200–4000	300–600
Energy capital cost ($/kWh)	5–430	2–120	200–250 [10]	600–3800	100–400

potentially lower environmental impact. However, one of the disadvantages of the CAES technology resides in its much lower energy density compared to the presented electrochemical solutions, meaning that equivalent installations would require more space. Another drawback of the CAES technologies is their lower Round Trip Efficiencies (RTEs) compared to electrochemical systems. However, economic considerations favor CAES systems due to their lower power and energy capital costs. Underground and aboveground CAES systems, for example, have energy capital costs ranging from $2 to $120 and $200 to $250 per kilowatt-h, respectively. Moreover, CAES systems generally have longer lifetimes, with both types lasting between up to 40 years, compared to the typical 5–15 years for electrochemical systems.

In its elementary form, a CAES system operates as follows: during surplus energy periods, electricity is used to power a motor that drives a compressor. This compressor then compresses ambient air into a storage reservoir. When there is a demand for electricity, the compressed air from the reservoir is released and directed to a turbine. The turbine converts the air's pressure energy into rotary motion, which is then used to drive a generator to produce electricity. Compressed air storage can be achieved through two distinct methods: underground and aboveground, as outlined in [12]. Underground storage utilizes natural caverns or excavated reservoirs in depleted mines, offering significant capacity and reduced construction costs [13]. Aboveground storage uses rigid tanks, providing flexibility in location but with higher manufacturing costs [14].

The practical applications of CAES systems encompass a variety of grid services [13]. These include peak shaving, where stored energy is released during high-demand periods to reduce the strain on the grid, and black start services, which provide power to restart a grid after a blackout. CAES systems support energy arbitrage by storing energy when prices are low and selling it when prices are high. Additionally, they are also employed for load shifting, which involves storing energy during low-demand periods and releasing it during peak times. Furthermore, CAES is increasingly integrated with intermittent renewable energy sources to manage variability and ensure a reliable power supply.

Government policies play a crucial role in the advancement and integration of energy storage technologies, including CAES. [15] reviews state-level policies on electrical energy storage in the United States, highlighting that since California's 2013 energy storage mandate, 14 other states have introduced policies to either facilitate operational experience with EES or reduce barriers to future deployments. His study presents a taxonomy of state policies and provides examples of their impact, such as policy interventions in Washington and California's progress in meeting energy storage targets. The author concludes that state policies significantly drive EES growth, supported by trends in cost declines and increasing storage deployments.

Nowadays, various classes of CAES systems are extensively reviewed in scientific literature. Budt et al. [4] provided a thorough overview of CAES approaches, classifying and comparing different CAES processes and their historical development. They evaluated the strengths and weaknesses of various CAES concepts and discussed the importance of accurate fluid property data for CAES design. Dooner and Wang [13] discussed the fundamental principles of CAES technology, including its grid-scale applications and the operational characteristics of existing CAES plants, such as those in Huntorf, Germany, and McIntosh, Alabama. Their book chapter also covered the economic and technical aspects of CAES, including a comparison with other energy storage technologies. Wang et al. [16] reviewed current research trends in CAES and its advantages, such as sustainability and low maintenance, highlighting the role of CAES in addressing challenges related to renewable energy integration and grid reliability. These reviews cover a range of CAES derivatives, including Liquid Air Energy Storage (LAES), Underwater CAES (UW-CAES), and Trigenerative Compressed Air Energy Storage (T-CAES). While the literature extensively covers these variants, the three primary classes that serve as foundational frameworks are:

- Diabatic CAES (D-CAES).
- Adiabatic CAES (A-CAES).
- Isothermal CAES (I-CAES).

D-CAES, representing the first generation of compressed air energy storage technology, incorporates air coolers after each compression stage to facilitate multiple stages of compression and air storage. This design aims to enhance efficiency by utilizing gas heaters before the expansion phase, which adds thermal energy to improve the generated energy [13]. Consequently, the RTE for D-CAES systems is calculated considering the thermal energy added [17]. The second generation of D-CAES further refines this approach by incorporating a heat exchanger at the turbine outlet, where temperatures can reach several hundred degrees Celsius, leveraging excess heat for preheating and thereby improving overall efficiency [4].

The practical applications of D-CAES technology illustrate its evolving efficiency. The pioneering Huntorf power station in Germany, operational in the 1970s, stored compressed air at 72 bar in underground salt caverns and generated 321 MW for two hours, achieving an RTE of 42 % [4]. Building on these advancements, the McIntosh plant in the USA, commissioned in the early 1990s, demonstrated significant progress by storing compressed air in a salt cavern and generating 110 MW for 24 h with an improved RTE of 54 % through effective heat recovery [4]. Looking to the future, the Berthel plant under construction in Texas aims to further enhance D-CAES capabilities. Scheduled for completion by 2025, this facility is designed to deliver 324 MW for 48 h, with specific efficiency details expected upon project completion [18].

A-CAES, representing the third generation of CAES technology, significantly enhances efficiency by recovering thermal energy after each compression stage for subsequent use before expansion. This advancement eliminates the need for a gas burner, optimizing energy use [13]. The incorporation of independent Thermal Energy Storage (TES) has further improved this technology, achieving a maximal theoretical RTE of 70 % [4].

Practical applications of A-CAES technology have varied in success. The ADELE project in Germany, a collaborative effort between RWE Power, General Electric, and other partners, aimed to become the first commercial A-CAES system with a proposed capacity of 300 MW. The project was designed for nearly four hours of underground energy storage, targeting an RTE of 70 % [19]. Unfortunately, financial constraints led to the project's abandonment [20]. In contrast, the TIC-500 project in Wuhu, China, which ran from 2012 to 2014, featured an experimental aboveground 500 kW A-CAES system with a water-based TES. Despite advanced heat exchange strategies, this project achieved a lower RTE of 33 % [21]. The commercial viability of A-CAES technology has been demonstrated by Hydrostor's 2019 launch of the world's first commercial A-CAES plant in Goderich, Canada. This facility, located in an old salt mine, has a power capacity of 1.75 MW and a storage capacity of 10 MWh. It is designed to manage peak demand periods, providing power to 2,000 residences for up to five hours. The Goderich plant reports an RTE ranging between 60 and 65 % [22]. Hydrostor is also advancing large-scale CAES projects in California (USA), Australia, and Britain [23].

The fourth generation, I-CAES, aims for quasi-isothermal compression/expansion, maintaining nearly constant temperature in the process. While achieving perfect isothermality is impractical, quasi-isothermal transformations can significantly improve efficiency. Recent research proposes using water vaporization directly in pistons for quasi-isothermal expansion, demonstrating a potential theoretical RTE of 80 % [4]. The sole documented I-CAES demonstration project is attributed to the American company SustainX. In 2013, SustainX initiated a 1.5 MW pilot project showcasing quasi-isothermal compression and expansion technology. To enhance system efficiency, a homogeneous mixture of water and air is injected directly into the compression and expansion equipment to augment heat exchange within [24]. Focused on isothermal technology demonstration, the project employs a

small 1 MWh above ground air storage system. However, the company asserts its system's compatibility with various storage types. The system was supposed to achieve an RTE of 54 % but got discontinued.

While examining the above stated CAES technology reviews, it can be observed that the majority of documented CAES projects focus on underground storage in caverns. This approach enables substantial energy storage but is constrained by geological considerations [5]. However, a few ventures take a different path, exploring aboveground storage solutions using rigid tanks. This approach, while offering lower energy capacity, provides flexibility for geographic installation [13], making it suitable for remote areas and potential integration within buildings. Additionally, aboveground storage, leveraging higher pressures in rigid reservoirs, demonstrates superior energy density [4].

Several methods have been developed to model and characterize aboveground CAES with experimental setups. Chen et al. [25] propose a modeling method for creating a comprehensive aboveground CAES system model. The reliability of this model is validated through tests on a laboratory-scale workbench, including a 3.2 kW scroll expander. The validation revealed a Mean Absolute Percentage Error (MAPE) consistently below 8 %. The experimental results and models indicate that the expander's output performance and the RTE vary across different configurations. The derived model suggests optimal conditions, highlighting a significant enhancement in RTE with an increased number of expander stages. The designed experimental setup exhibits RTE ranging from 13 % to 25 % under different conditions, with the optimal RTE projected to reach 60 % for a triple-stage system. Similarly, Dib et al. [26] explored a numerical model of a small high-pressure A-CAES system (200 bar) with TES, possessing a capacity of 188 kWh. This model was developed based on commercially available equipment. While lacking experimental validation, the study facilitated a thorough analysis of the scenario in which the CAES system was integrated with photovoltaic solar panels for a building application. The outcomes revealed a RTE of 30.0 % for the storage system. Cheayb et al. [27] developed a model of a high-pressure CAES with a trigenerative configuration, followed by experimental validation. The experimental setup was able to generate a model and characterize power of 0.435 kW for 1.66 h, resulting in a 0.72 kWh capacity for an initial discharge state of 300 bar. The primary objective was to assess the performance of such a system when integrated with a building structure. The results of the experimental validation showed a maximum relative error of 13.2 %. Considering that the compression heat is not used at the expansion process, the experimental system showed a low RTE of 3.6 %. Even when considering the heating and cooling potential for a building application, the RTE reached nearly 16 %.

Despite the theoretical potential for advanced concepts such as A-CAES and I-CAES to achieve maximal RTEs of 70 % and 80 %, respectively, experimental results from smaller aboveground CAES projects have faced difficulties in approaching these figures. These challenges in achieving higher RTEs stem from several factors, including inadequate or absent compression heat recovery, suboptimal efficiencies at the component level, and the necessity for a pressure regulator, which introduces additional irreversibilities within the system. This indicates a significant gap between theoretical models and practical implementations, necessitating further research and development to bridge this divide.

The novelty of this study resides in its multifaceted contributions to the relatively underexplored domain of aboveground CAES. The key contributions of this research are as follows:

- **Development of a fully instrumented test bench**: In light of the limited existing literature, a fully instrumented test bench dedicated to aboveground CAES has been assembled. This setup significantly enhances the empirical understanding of aboveground CAES systems, unlike the models which lack experimental validation.
- **Advanced numerical model**: The proposed model integrates real air properties and accounts for heat transfer dynamics, deviating

from conventional practices seen in [25,26,27]. This approach ensures a more accurate representation of the system's behavior under diverse ambient conditions, aiming to improve model accuracy in mimicking real system behavior.
- **Modeling transient dynamics**: A quasi-steady-state approach to model the transient dynamics of the system, partitioning calculations into smaller intervals characterized by steady-state conditions. This method allows us to consider changes in ambient conditions over time, providing a dynamic simulation of the system's response, which is an improvement over the steady-state assumptions used in other reviewed studies [25,26,27].
- **Parametric analysis**: The study includes a parametric analysis within the numerical model, systematically refining the system's behavior and exploring various variables. This analysis identifies areas for improvement and proposes targeted enhancements, setting the stage for further optimization of aboveground CAES systems.

These contributions collectively advance the empirical and theoretical understanding of aboveground CAES, marking a significant step forward in the development of this promising technology.

Therefore, this study hypothesizes that the development of a fully instrumented test bench and an advanced numerical model, integrating real air properties and accounting for heat transfer dynamics, will significantly improve the model capability in representing the real behavior of CAES systems by minimizing errors. It is further hypothesize that this improved model will enable a detailed parametric analysis, which will help identify specific opportunities for system improvement. These comprehensive efforts collectively contribute to advancing the empirical and theoretical understanding of aboveground CAES, marking a significant step forward in the development of this promising technology.

2. Materials and methods

The primary aim of this study is to undertake a combined experimental and simulation analysis of an aboveground CAES system, with the goal of pinpointing opportunities for improvement. To achieve this goal, it has been divided into three sub-objectives: (1) run an experimental campaign to acquire data; (2) develop a comprehensive CAES model representing the experimental setup; (3) conduct a parametric analysis to identify improvement opportunities.

2.1. Experimental set-up and data acquisition

A fully instrumented CAES workbench will be established to collect experimental data. This endeavor serves a dual purpose: first, to quantify the system's performance and thoroughly comprehend its behavior, and second, to determine unknown parameters. Data will be collected at one-second intervals to ensure precise capture of system dynamics. Simultaneously, ambient air conditions will be recorded to establish the baseline scenario for subsequent simulations. This dataset will provide a robust foundation for the simulation and calibration of the model.

The experimental setup, developed in partnership with Hydro-Québec's research institute (IREQ), comprises a test bench housed in a 20-foot metal container (Fig. 1). This container is divided into two distinct sections by an insulating partition. The left section accommodates the compression system, comprising a 45 kW compressor (1), a control unit (2), and an adsorption dryer (3). Acoustic insulation minimizes sound emissions, while ventilation ducts ensure forced air circulation to avoid overheating. On the right, this section operates as a storage system for compressed air. A total of 12 reservoirs (4) with a capacity of 0.27 m^3 and 8 reservoirs (4) with a capacity of 0.32 m^3 are connected in a parallel configuration, resulting in a combined volume of 5.86 m^3. Outside of the container, a pressure regulator (5) maintains a constant output pressure. It's important to note that, due to time constraints, the final expansion system has not been included and will only
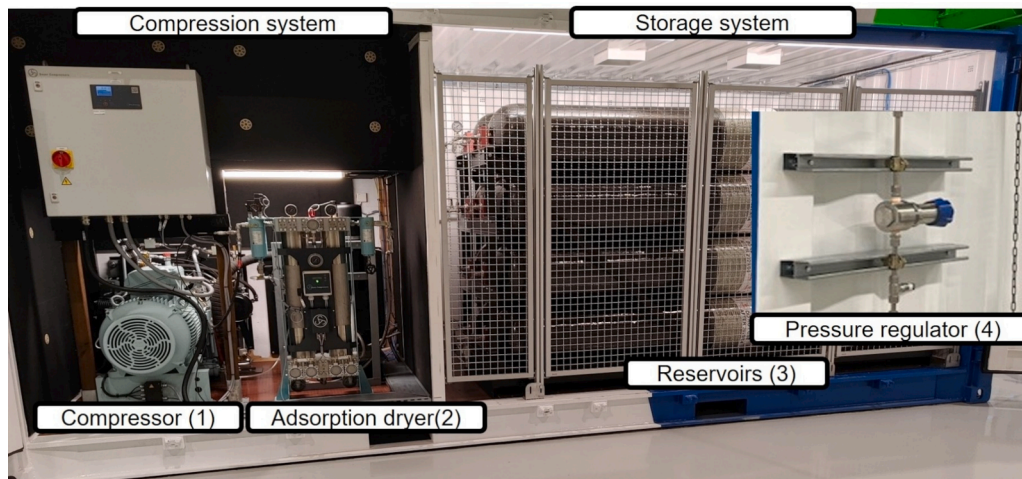
Fig. 1. Photograph of the test bench installation.

be modeled. Despite this, the test bench is fully instrumented, allowing for a thorough analysis of the system.

The 45 kW volumetric compressor, labeled (1) in Fig. 1, comprises a four-stage air-cooled compressor designed to elevate pressure up to 350 bar. However, for experimental purposes, the maximum pressure will be constrained to 190 bar. The first piston compresses 1.61×10^{-3} m^3 of air with each rotation of its crankshaft, which rotates at a speed of 1782 rpm, resulting in a volume flow of 172.4 m^3/h. The compressor incorporates an integrated dehumidifying process to ensure the air's moisture content is minimized. Ensuring moisture-free air in the reservoir is crucial for two key reasons: even minimal water content can degrade downstream equipment during the discharge process, affecting instrumentation, reservoirs, and the expansion system, and air expansion during power generation may lead to a significant temperature drop, risking ice or frost formation with destructive consequences. To mitigate this, an adsorption dryer (labeled [3] in Fig. 1) is installed between the compressor (1) and the air reservoirs (4). Limited technical details are available, but the manufacturer notes a flow loss of 20–25 % during the drying process, a parameter to be verified experimentally. Further technical details regarding the compressor and the intercooler can be found in the Supplementary Material (Table 7), which offers supplementary information on the key components utilized in this study. The reservoirs (labeled [4] in Fig. 1), although their exact composition is undisclosed by the supplier, are constructed with an inner layer of 6061-T6 aluminum alloy and an outer layer of carbon fiber. Technical specifications for the reservoirs are detailed in Table 8 in Supplementary Material. Material properties for the aluminum alloy were sourced from the ASM handbook [28]. For carbon fiber properties, estimates were based on key studies such as Ou et al. [29], who detailed the mechanical properties of carbon fiber composites, and Khan et al. [30], who investigated the use of carbon fiber reinforced plastic in various applications, providing insights into its thermal and mechanical behavior.

The pressure regulator, labeled as (5) in Fig. 1, ensure a steady output pressure independent of reservoir fluctuations. This function guarantees a consistent input parameter for the future operation of a turbine dedicated to power generation. The regulator is adjustable for output pressures between 17 and 275 bar, offering tailored flexibility to operational requirements. However, it's essential to recognize the pressure regulator's limitations. The observations reveal challenges in maintaining a constant output pressure when the input pressure difference is below 15 bar. Consequently, the system will automatically shut down if the pressure in the reservoir drops below this threshold.

For simulation purposes, it is proposed to utilize three air turbines connected in series, sourced from DEPRAG company. The key characteristics of this equipment are detailed in Table 9 available in the

Supplementary Material section. It is essential to highlight that in this configuration, the three air turbines connected in series would require preheating of the air to temperatures of 130 °C, 90 °C, and 90 °C for stages 1, 2, and 3, respectively. This preheating is crucial for attaining the specified performance, resulting in a cumulative electrical power generation of 62 kW.

The acquisition of experimental data holds triple importance for the project, enabling quantitative analysis of the system's performance, obtaining missing parameters, and playing a crucial role in model calibration. The test bench is equipped with dedicated sensors, allowing determination of the air's state at each point in the system. A complete scheme of the test bench showing the positioning of each instrumentation is available in Fig. 2.

2.2. Development of the model

The Python programming language was selected for its flexibility and the availability of free numerical tools included in libraries such as NumPy [31], SciPy [32], Pandas [33], Matplotlib [34], and CoolProp [35]. In CAES modeling, understanding the air's state during transformation relies on state equations. While the ideal gas equation is commonly used for its simplicity [36] in all reviewed models [25,26,27,37], caution is warranted during CAES compression processes with substantial pressure and temperature increases [4]. To ensure accurate determination of real air thermodynamic properties without unnecessary approximation, the semi-empirical formulation for dry air by Lemmon et al. [38] is seamlessly integrated within CoolProp. This integration addresses potential errors associated with ideal gas assumptions, enhancing precision in the model. The model adopts a quasi-steady-state approach, incorporating transient heat transfer into the storage system modeling. It leverages CoolProp for accurate modeling of high-pressure dry air. General assumptions include:

- Air is considered moisture-free due to the dehumidification process and adsorption air dryer.
- Pressure losses are negligible, and piping is isolated.
- Variations in potential and kinetic energy are negligible compared to enthalpy changes.

In this investigation, compression and expansion are represented through a polytropic transformation, which generalizes reversible transformations, as governed by the fundamental equation (1) as seen in [39]. A polytropic transformation typically involves a polytropic index (n) ranging between 1 and γ, the specific heat ratio, signifying either a cooled compression or a heated expansion process.
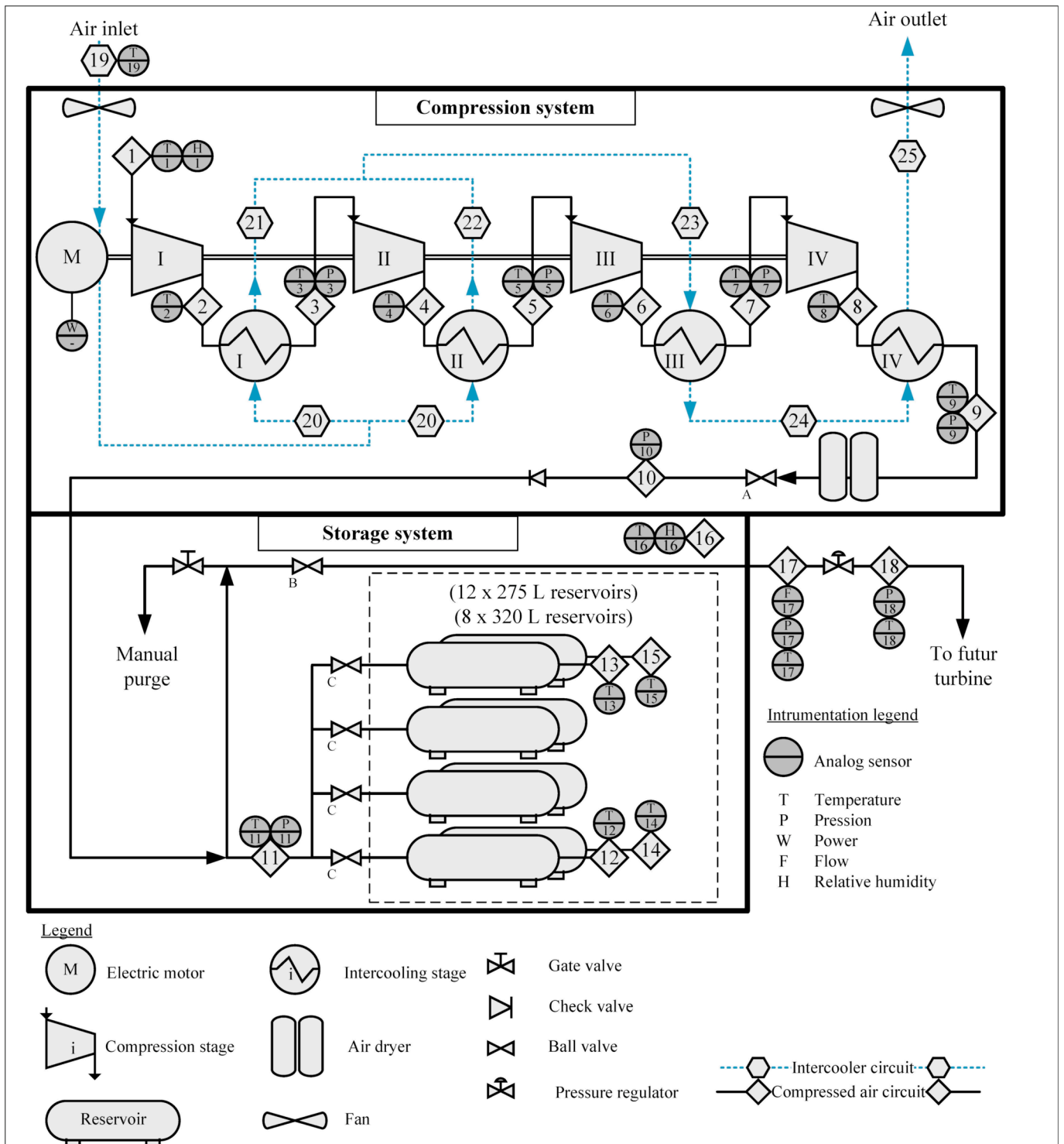
Fig. 2. Schematic view of the CAES system with instrumentation emplacements and identification.

$$P_{in}v^n_{in} = P_{out}v^n_{out} = Pv^n = Cte \qquad (1)$$

2.2.1. Modeling of the compressor

Fig. 3 presents a schematic view of a compressor stage accompanied by a labeled nomenclature designed to enhance comprehension.

By rearranging the Eq. (1), the specific volume at the outlet of the compression stage can be expressed as follows:

$$v_{c,out,i} = v_{c,in,i} \cdot \beta_{c,i}^{\frac{-1}{n_{c,i}}} \left[\mathrm{m^3/kg} \right] \qquad (2)$$
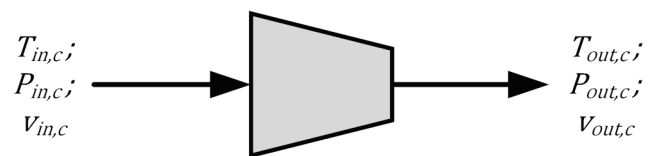

Fig. 3. Schematic view of a compressor stage.

The coefficient $\beta_{c,i}$ thus quantifies the compression ratio for the respective stage and is defined as the ratio between the absolute outlet pressure $P_{out,c,i}$ and the absolute inlet pressure $P_{in,c,i}$ for stage *i*. It is calculated according to the Eq. (3) as per [40]:

$$\beta_{c,i} = \frac{P_{out,c,i}}{P_{in,c,i}} \tag{3}$$

Considering the assumption that variations in kinetic and potential energies are negligible compared to other variations ($\Delta ke = \Delta pe \approx 0$), the specific polytropic work of compression for one stage *i* can be represented by the Eq. (4) according to [39]:

$$w_{pol,c,i} = \frac{n_{c,i}}{n_{c,i} - 1}\left(P_{out,c,i}v_{out,c,i} - P_{in,c,i}v_{in,c,i}\right)[\text{J/kg}] \tag{4}$$

Now, considering *Nc* as the amount of compression stages, the total compression work ($W_{c,tot}$), can be formulated as the cumulative sum of the polytropic specific work ($w_{pol,c,i}$), for each individual stage scaled by the mass flow rate ($\dot{m}_c$), according to [39,40]. Then the total electric power ($\dot{W}_{el,c,tot}$) can be obtained by considering both electrical (η_{el}) and mechanical (η_{mec}) efficiency definitions, as shown in Eq. (5).

$$\dot{W}_{el,c,tot} = \frac{1}{\eta_{mec,c} \cdot \eta_{el,c}} \dot{m}_c \sum_{i=1}^{N_c} \frac{n_{c,i}}{n_{c,i} - 1}\left(P_{out,c,i}v_{out,c,i} - P_{in,c,i}v_{in,c,i}\right)[\text{W}] \tag{5}$$

2.2.2. Modeling of the intercooling system

Fig. 4 illustrates a schematic representation of a heat exchanger stage, featuring a labeled nomenclature designed to improve understanding.

Here, the subscripts *hot_he* and *cold_he* are introduced to designate the hot and cold sides of the heat exchanger stage. The method adopted for the development of the cooling system is based on the Number of Transfer Units (NTU) method [41], also known as the efficiency method. The following assumptions are considered for the heat exchanger model:

- The mass flow rates of the hot and cold fluids are constant during a time step Δt.
- The pressure drop between the outlet and the inlet of the heat exchanger is negligible.

In this study, the geometry of the heat exchangers constituting the cooling system remains unknown and would require considerable time to be determined. However, the inlet and outlet conditions can be measured experimentally using available instrumentation. The efficiency of the heat exchanger can be established experimentally using relation (6) based on [41]:

$$\eta_{he,i} = \frac{\dot{Q}_{he,i}}{\dot{Q}_{max,he,i}} = \frac{\dot{C}_{he,i}\left(T_{in,he,i} - T_{out,he,i}\right)}{\dot{C}_{min,he,i}\left(\Delta T_{max,i}\right)} \tag{6}$$

Where $\dot{C}$ is the heat capacity flow rate in W/K for the hot or cold fluid. This is obtained by multiplying the specific heat capacity (c_p) of the fluid
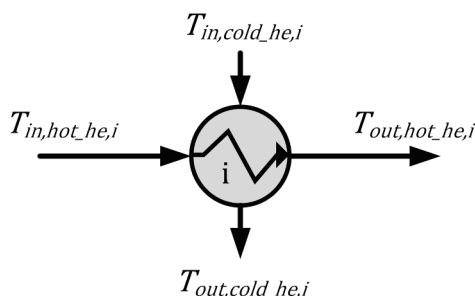
by the mass flow rate ($\dot{m}$) of the respective fluid. $\dot{C}_{min}$ here represents the minimum result between $\dot{C}_{hot}$ and $\dot{C}_{cold}$ as proposed in [41]. However, since the specific heat capacity is not constant and is a function of the fluid temperature, the heat transfer rate for each stage ($\dot{Q}_{he,i}$) can be determined following the integral Eq. (7) [41].

$$\dot{Q}_{he,i} = \dot{m}_{he,i} \int_{T_{in,he,i}}^{T_{out,he,i}} cp_{he,i}(T)dT[\text{W}] \tag{7}$$

Moreover, due to the significance of the mass flow rate of the cold fluid, it has been evaluated that $\dot{C}_{min}$ will always be $\dot{C}_{hot}$. Thus, Eq. (6) can be rearranged into Eq. (8) to obtain the outlet temperature on the hot side for each heat exchanger *i* as seen in [39].

$$T_{out,hot\_he,i} = T_{in,hot\_he,i} - \eta_{he,i}\left(T_{in,hot\_he,i} - T_{in,cold\_he,i}\right)[\text{K}] \tag{8}$$

The total heat transfer rate of the intercooler corresponds to the sum of the heat transfer rate from each stage as shown in the Eq. (9):

$$\dot{Q}_{he,tot} = \sum_{i=1}^{N_c} \dot{Q}_{he,i}[\text{W}] \tag{9}$$

2.2.3. Modeling of the adsorption air dryer

The use of an adsorption air dryer results in a decrease in the mass flow rate due to the regeneration process of the adsorbent material, where air sourced from the compressor is employed. This phenomenon will be quantified through a model based on its efficiency (η_{dryer}).

$$\dot{m}_{out,dryer} = \dot{m}_{in,dryer} \cdot \eta_{dryer}[\text{kg/s}] \tag{10}$$

While the pressure and temperature at the inlet and outlet remain constant, the dryer efficiency, determined experimentally, is established at a value of 81 %. This value aligns with the range provided by the compressor manufacturer, indicating a mass flow loss of between 20 % and 25 %.

2.2.4. Modeling of the reservoir system

The assumptions related to the reservoirs are formulated as follows:

- The temperature gradient inside the reservoirs will be considered uniform as seen in [25].
- Heat transfer by radiation is negligible compared to other modes of transfer. Similar assumption has been made by [27].
- An equivalent reservoir representing the combined geometry of individual reservoirs is assumed.
- The storage volume will be considered constant.

The energy balance on the control volume represented by an equivalent reservoir can be illustrated by Fig. 5.

The total volume and heat exchange surface of the equivalent reservoir will be determined using a multiplication factor based on the quantity of 320 L and 275 L reservoirs, as specified in Eqs. (11) and (12).

$$V_{equivalent} = V_{320} \times N_{320} + V_{275} \times N_{275}[m^3] \tag{11}$$

$$A_{equivalent} = A_{320} \times N_{320} + A_{275} \times N_{275}[m^2] \tag{12}$$

The changes in internal energy within the reservoir can be analyzed

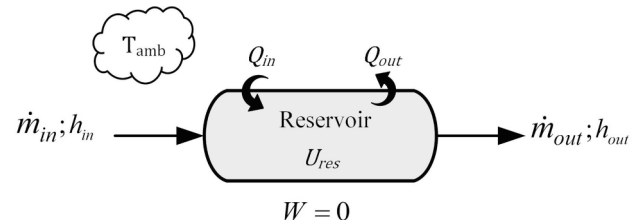**Fig. 4.** Schematic view of a heat exchanger stage.

Fig. 5. Mass and energy balance scheme on the reservoir for the filling phase.

by applying the energy balance [39], expressed differentially as in Eq. (13).

$$dU = \partial H - \partial Q \, [\text{J}] \tag{13}$$

This assumes that variations in kinetic and potential energies are insignificantly small compared to other energy forms and acknowledges the absence of work in the reservoir as seen in the work of [25]. This equation can be further developed into a more explicit form as expressed in Eq. (14), considering a timestep Δt.

$$\Delta U = \dot{m}_{in} h_{in} \Delta t - \dot{m}_{out} h_{out} \Delta t - KA(T_{res} - T_{amb}) \Delta t \, [\text{J}] \tag{14}$$

The concept of overall heat transfer coefficient (K) serves to unify the different modes of heat transfer into a single concept. Among these modes, thermal conduction, thermal convection, and thermal radiation are distinguished.

2.2.5. Modeling of the pressure regulator

Fig. 6 presents a schematic view of the pressure regulator with its designed nomenclature.

It will be assumed that the air conditions at the entrance match those at the exit of the reservoir system. According to [36], the evolution of the fluid within a pressure regulator is assumed to be adiabatic, justified by the limited air available for thermal exchange. Furthermore, there is no work performed ($W = 0$), and the variations in kinetic and potential energies are deemed negligible. Consequently, a constant enthalpy model will be assumed for this component ($h_2 \cong h_1$) [36].

In addition to this assumption, a second model retrieved from Cheayb et al.'s study [27], which employs a semi-empirical relation grounded in Hoxton's work [42], will also be evaluated. This relation (15) is validated for pressures within the 25–150 bar range. Despite the operating pressure exceeding this range (190 bar), the model will still be assessed for the sake of comparison in Section 3.2.

$$T(P) = a \cdot P^2 + b \cdot P + c \, [\text{K}] \tag{15}$$

Here, the constants a, b, and c are determined as follows:

$$a = \frac{1}{2}\left(\frac{0,0297}{T_{in}} - \frac{1,674}{T_{in}^2} - \frac{19093}{T_{in}^3} + 0,0000157 \right)$$

$$b = \frac{50,1}{T_{in}} + \frac{14830}{T_{in}^2} + \frac{366000}{T_{in}^3} - 0,122$$

$$c = T_{in} - a \cdot P_{in}^2 - b \cdot P_{in}$$

It's essential to note that, specifically in relation (15), pressure is denoted in bar, and temperature is measured in Kelvin.

2.2.6. Modeling of the expansion device

Fig. 7 illustrates a schematic representation of an expansion stage, featuring a labeled nomenclature.

The equations describing the expansion process rely on the same polytropic process used for compression, as seen in Eq. (1). Therefore, the same equations will be utilized, maintaining consistent nomenclature for both compression and expansion.

$$v_{e,out,i} = v_{e,in,i} \cdot \beta_{e,i}^{\frac{-1}{n_{e,i}}} \, [\text{m}^3/\text{kg}] \tag{16}$$
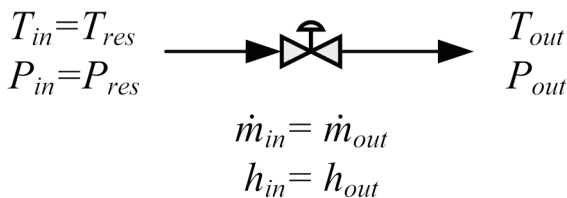
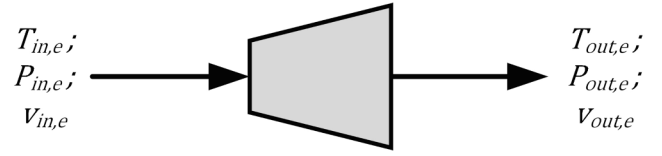**Fig. 6.** Mass and energy flow scheme of the pressure regulator.

Fig. 7. Schematic view of an expansion stage.

$$\dot{W}_{el,e,tot} = \eta_{mec,e} \eta_{el,e} \dot{m}_e \sum_{i=1}^{N_e} \frac{n_{e,i}}{n_{e,i}-1}\left(P_{out,e,i} v_{out,e,i} - P_{in,e,i} v_{in,e,i} \right) [\text{W}] \tag{17}$$

The model relied on several assumptions and simplifications, such as idealized heat transfer dynamics and steady-state conditions for certain parameters. These assumptions, while necessary for model feasibility, may limit its ability to accurately represent more complex real-world scenarios. The integration of real air properties and dynamic heat transfer still involves approximations that may impact the model's accuracy.

2.3. Model calibration

In pursuit of this sub objective, a model calibration will take place with the goal of improving the model's predictive capability in replicating the actual system dynamics. The evaluation process entails comparing the model's predictions with the experimental measurements, employing two statistical metrics: the Root Mean Squared Error (RMSE) and the Mean Absolute Percentage Error (MAPE). These metrics serve to gauge the model's precision in mimicking the authentic behavior of the system. Eqs. (18) and (19) will be instrumental in computing these metrics, where $\hat{y}_i$ denotes the value predicted by the model, y_i the experimental value and N_{sample} the sample size.

$$RMSE = \sqrt{\frac{\sum_{i=1}^{N_{sample}} (\hat{y}_i - y_i)^2}{N_{sample}}} \tag{18}$$

$$MAPE = \frac{1}{N_{sample}} \sum_{i=1}^{N_{sample}} \left| \frac{y_i - \hat{y}_i}{y_i} \right| \times 100 \tag{19}$$

The calibration process involves four key steps aimed at enhancing the model's performance, involving parameter optimization. Initially, uncertain parameters within the model are identified. These parameters typically correspond to those not explicitly defined in the technical component descriptions and will be subject to a calibration.

The next step involves formulating an objective function based on the known experimental values. This objective function serves as a benchmark for the model's predictions and establishes a quantifiable metric against which the model's accuracy is assessed. The optimization process is then conducted using numerical optimization tools from the Python Scipy library, specifically the Broyden-Fletcher-Goldfarb-Shanno (BFGS) algorithm. The primary goal of this process is to minimize the RMSE between experimental and simulation results.

The selection of parameters for the BFGS algorithm, including the initial guess for the parameters, convergence tolerance, and step size, is a crucial aspect of this process. These parameters are chosen based on empirical methods, which involve using established guidelines from the literature and experiences with similar optimization problems. Experimental tuning is also employed, where parameters are adjusted through preliminary tests to assess their impact on convergence speed and accuracy.

Constraints relevant to the model, such as physical limits or operational boundaries, are incorporated into the optimization process. These constraints are mathematically formulated and managed using warning generation functions, which are applied to the main model to discourage infeasible solutions. Feasibility checks are also performed at each iteration to ensure that constraints are respected throughout the optimization process.

Upon completing the optimization, calibrated values for uncertain parameters are obtained. These values represent the refined parameters that optimize the model's predictive capabilities, aligning it more closely with real-world observations. The model's performance is subsequently evaluated by comparing experimental and simulation outcomes using a distinct dataset from separate experiments. During this evaluation phase, transient visual representations and statistical metrics are employed to rigorously assess the model's accuracy and reliability.

It is noteworthy that the datasets used for calibration and model's performance evaluation were limited in size and scope. Although efforts were made to collect representative data, the dataset may not encompass all potential operational scenarios, which could affect the generalizability of the model's predictions.

2.4. Parametric analysis

The parametric analysis will be presented in Section 3.3 of this study. This analysis aims to highlight the flaws and the potential improvement that could be applied to the experimental workbench. In this study, the performance criterion will be exclusively centered on the RTE, expressed by equation (20).

$$RTE_{CAES} = \frac{E_{produced}}{E_{consumed}} \qquad (20)$$

The selected parameters for this analysis, determined based on identified improvement avenues during the literature review, include ambient temperature, reservoir maximum pressure, and the polytropic index. The analysis will focus on two distinct system configurations. Firstly, a CAES system without preheating, which mirrors the current experimental setup and serves as the baseline configuration, will be simulated. In this configuration, the compression heat is not utilized during the expansion process. Secondly, the potential benefits of preheating the air before it reaches the turbine stages will be identified. To do so, the temperature parameter will be adjusted to meet the nominal requirements of the turbine characteristics. Then, the effect of increasing the amount of expansion stages will be explored. Finally, the feasibility of achieving these nominal temperatures by reintroducing the compression thermal energy extracted during the compression process before the turbine stage will be assessed. This analysis aligns with the concept of A-CAES, utilizing a TES system to store the compression heat.

3. Results and discussion

This section is organized into three subsections: the experimental campaign, calibration and performance, and parametric analysis. Each subsection will present and discuss the results corresponding to these key aspects of the study.

3.1. Results of the experimental campaign

The experimental campaign comprised two distinct tests representing the charge and discharge phases. Throughout these tests, continuous data acquisition of the air state was performed every second using the instrumentation depicted in Fig. 2. The charge phase experiment aimed to fully charge the air reservoir to its maximum capacity of 5.86 m³, pressurizing it from atmospheric pressure to 190 bar over the duration of almost 10 h. This process consumed 396 kWh of electrical power, averaging 39 kW. Notably, the experiment allowed for the acquisition of compression ratios for each stage, as depicted in Fig. 8.

Upon examination of the results, the compression ratios for stages 1 and 2 exhibit a relatively stable pattern throughout the charging phase. In contrast, those for stages 3 and 4 demonstrate a linear increase beyond the 60-bar threshold within the reservoirs. This consistent behavior corroborates findings from previous experimental studies conducted by Cheayb et al. [27] and Wang et al. [43]. Consequently, the compression ratios have been calculated for stage 1 and stage 2 by
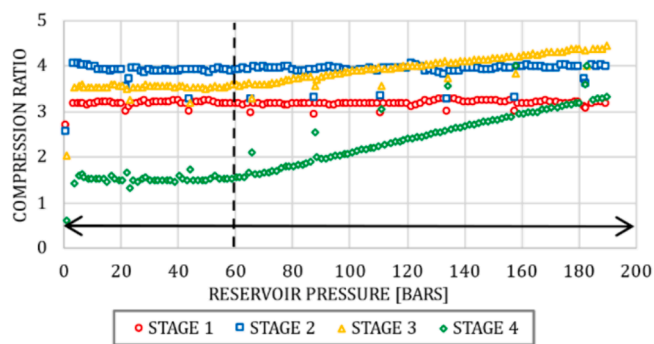

Fig. 8. Compression ratio for each stage based on reservoir pressure.

averaging the obtained results, resulting in values of 3.25 and 3.75, respectively. However, the compression ratios for stages 3 and 4 are subject to variations based on the pressure within the reservoirs, falling within the ranges of 3.54–4.44 and 1.52–3.5, respectively. Moreover, this experiment revealed insights into the loss of mass flow during the charging phase. By initially utilizing the recorded state of the air at the inlet of the compressor (point No. 1 in Fig. 2) and considering the compressor volume flow of 172.4 m³/h, the average mass flow entering the compressor was determined to be 0.052 kg/s. With the manufacturer's reported compressor outlet (point No. 9 in Fig. 2) mass flow at being 0.043 kg/s, the compressor exhibited an average volumetric efficiency of approximately 83 %. Subsequently, as the air progressed through the air dryer, further reductions in mass flow occurred due to the operational process of the equipment. An average mass flow of 0.032 kg/s at the outlet of the equipment has been experimentally determined (point No. 10 in Fig. 2). This value represents the mass flow entering the reservoir system. The cumulative mass flow loss of 0.02 kg/s, accounting for a 38 % decrease, prolongs the charging time needed to fully pressurize the reservoir system, impacting both energy consumption and system RTE. For the discharge phase experiment, the reservoir initiates at a partial capacity of 2.56 m³ with a pressure of 190 bar. The pressure regulator was set to maintain a steady delivery pressure of 35 bar and the test was stopped when the reservoir pressure reached 50 bar. This ensures a consistent flow and pressure throughout the phase. Initial readings indicated an average reservoir temperature of 55 °C, with the system taking 38 min to reach the pressure threshold of 50 bar. Mass flow was directly measured using a flow meter, recording an average discharge of 0.148 kg/s.

3.2. Results of the calibration and evaluation of the model performance

A first simulation was conducted to compare the model ability to mimic the real CAES system behavior. While some uncertain parameters where averaged from experimental data, some other where initially set based on the reviewed literature [25,26,27], therefore necessitating calibration. This has been done following the method outlined in Section 2.2.

The calibration of the charge phase allowed the adjustment of uncertain model parameters, enhancing the model's ability to accurately replicate the real CAES workbench behavior. To illustrate this process, Fig. 9 showcases the outlet temperature of the compressor's stage 4, showing the results obtained with non-calibrated and calibrated polytropic indexes. Additionally, the model's performance was evaluated using statistical metrics such as the RMSE (Root Mean Square Error) and MAPE (Mean Absolute Percentage Error) presented in Section 2.2.

The initial polytropic index of 1.59, determined from experimental data acquisition, was subsequently calibrated to a more representing value of 1.52. The calibrated data visually align more closely with the experimental trends, indicating an enhanced representation of the real system behavior. Furthermore, significant improvements in statistical
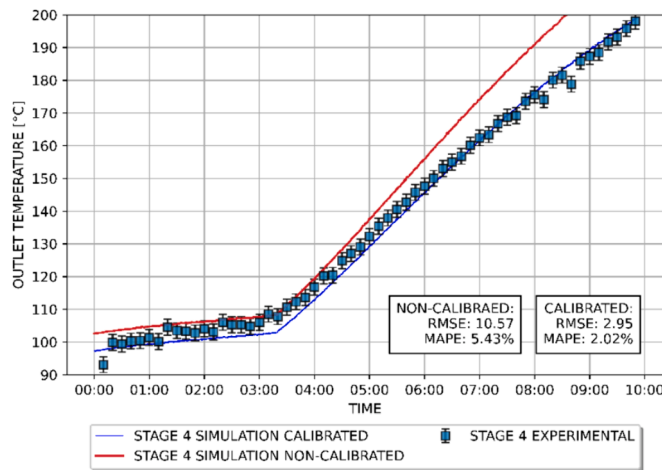
Fig. 9. Temperature at compression 4th stage outlet: Results before and after calibration.

indices affirm the efficacy of the calibration process in refining the model's predictive capacity. Specifically, the RMSE decreased from 10.39 °C to 2.83 °C, while the MAPE decreased from 5.49 % to 1.90 %. Further calibration was conducted for every other uncertain parameter. Resumed calibration results are provided in Table 2.

The calibration process resulted in minor changes overall, except for two parameters. Initially set at a constant value of 76 %, the intercooler efficiency introduced inaccuracies in simulating output temperatures at the fourth stage. Subsequently, a transient efficiency model was implemented, fluctuating between 74 % and 85 %, with efficiency scaling alongside reservoir pressure. Similarly, the mechanical efficiency, initially gleaned from literature [26,27], underwent calibration due to discrepancies between assumed and observed values. Ranging between 69 % and 74 % depending on reservoir pressure, the calibrated values suggested lower efficiency than previously indicated in literature (average 85 %).

Following the calibration of the global thermal heat transfer coefficient, the coefficient was determined to be K=8.8 W/m^2 K. In contrast, Chen et al. [35] experimentally derived a coefficient of 13.9 W/m^2 K for their reservoir system. This discrepancy suggests that the reservoir configuration tend to be less restrictive to thermal exchanges compared to the reference system. This variation in thermal behavior may be attributed to the distinctive design of the reservoir setup, where each individual reservoir interacts with others in a manner that influences heat exchange dynamics.

The calibration of the discharge of air into the reservoir system induces a notable temperature reduction, stemming from the rapid

Table 2
Calibration results for the charging phase uncertain parameters.

Uncertain parameters		Initial value	Calibrated value
Compressor			
Polytropic indexes	Stage 1	1.35	1.35
	Stage 2	1.37	1.38
	Stage 3	1.44	1.44
	Stage 4	1.59	1.52
Mechanical efficiency, [%]		85	69——74
Intercooler			
Efficiency, [%]	Stage 1	83	82
	Stage 2	86	85
	Stage 3	86	88
	Stage 4	76	74——85
Air reservoir system			
Global heat transfer coefficient, [W/m^2·K]		13.9	8.8

pressure drop. However, during the discharge phase, the comparison between experimental and simulation data revealed that the accumulated heat within the reservoir structure, acquired during the charging phase, influences the air temperature inside the storage.

In addressing the energy balance (Eq. (13)) within the reservoir structure, two unknown parameters emerge: the external convection coefficient ($h_{conv,ext}$) and the internal heat convection coefficient ($h_{conv,int}$), where the heat transferred by convection for a time step can be expressed by equation (21).

$$Q_{conv,x} = h_{conv,x} A_x (T_{structure} - T_x) \Delta t [J] \quad (21)$$

where the subscript x represents either the internal or external perspective of the reservoir structure. For this model, a uniform temperature distribution within the reservoir structure materials and a constant heat convection coefficient were assumed. The calibration results of the two unknown parameters reveal a ($h_{conv,ext}$) of 2.47 W/m^2 K and a ($h_{conv,int}$) of 25.42 W/m^2 K.

The acquisition of experimental data provided initial insights into the system's behavior and, crucially, enabled the collection of unknown parameters essential for the simulations. However, to achieve an extended evaluation of the model performance, the calibrated model should be compared to a different dataset.

In the endeavor to identify areas for improvement, a parameter analysis will be conducted focusing on the influence of multistage expansion on system performance. This decision was inspired by the findings of Chen et al. [25], who demonstrated a significant enhancement in the system's RTE through the integration of multiple expansion stages. The experiment will focus on analyzing the RTE for setups employing 1, 2, and 3 stages of expansion prior to the turbine parameters outlined in Table 9. It's important to note that the relevance of multistage expansion is contingent upon its conjunction with preheating. Therefore, the evaluation will exclusively focus on scenarios where multistage expansion is combined with preheating.

The incorporation of multiple stages affects the system in some ways. Primarily, multistage expansion facilitates a greater combined expansion ratio, thereby augmenting power generation capabilities. However, this also increases the minimum working pressure required by the turbine. Consequently, if the compressed air reservoir pressure falls below this minimum threshold, the discharge phase will be disrupted, resulting in a dead mass of air within the system. This accumulation adversely affects both the charging and discharging phase duration. Analysis of the charging results indicates that while the compressor workload remains constant regardless of parameter variations, both the charging time and energy consumption are affected. Specifically, as the working pressure rises with additional expansion stages, the energy consumed during charging decreases from nearly 380 kWh to 290 kWh as the number of stages increases from 1 to 3. Fig. 16 present simulation results for varying the expansion stages from 1 to 3.

In this section, the evaluation of the model's performance against experimental data is presented. By thoroughly assessing the agreement between the model and an independent dataset obtained from a separate experiment, confidence in its accuracy to simulate the system's behavior is enhanced. This thorough evaluation step is crucial before proceeding with parametric analysis. Table 3 summarizes the statistical indices obtained from both experimental and simulation data for the charging phase, providing a quantitative assessment of the agreement between the two datasets. Additionally, Fig. 10 illustrates a comparison between the simulated and experimental data for power and energy generation during the charging phase, offering a visual example of the validation results.

Upon analyzing the performance evaluation results, a close agreement between the simulated and experimental data was observed, as indicated by low RMSE and MAPE values across various parameters and stages, with the highest MAPE of 3.58 %. The plot depicted in Fig. 13. Further confirms this agreement, showing a strong correlation between

Table 3
Statistical indices results for the charging phase.

Parameters			RMSE	MAPE
Compressor				
Temperature output, °C		Stage 1	2.29	1.16 %
		Stage 2	3.30	1.38 %
		Stage 3	3.17	1.20 %
		Stage 4	2.95	2.03 %
Electrical power, kW			1.85	3.58 %
Cumulated consumed energy, kWh			6.24	2.52 %
Heat exchangers				
Temperature output, °C		Stage 1	1.80	2.80 %
		Stage 2	1.25	1.87 %
		Stage 3	1.03	1.66 %
		Stage 4	1.02	1.63 %
Air reservoir system				
Temperature, °C			0.17	0.38 %
Pressure, bar			1.57	1.74 %
Air mass, kg			8.85	1.56 %
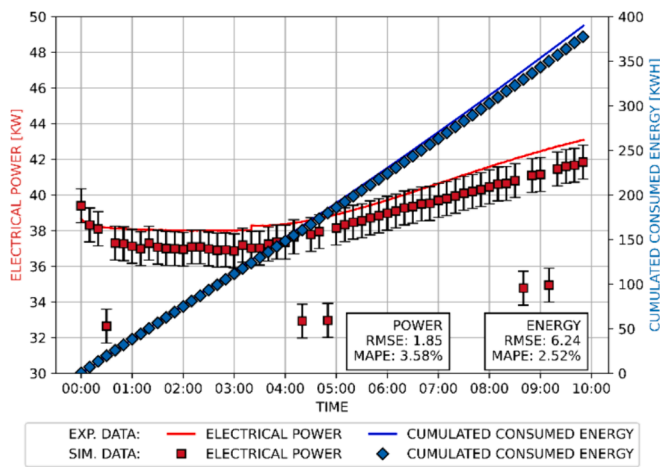
Fig. 10. Visual representation of the electrical power and cumulated consumed energy for validation.

simulated values (illustrated by the full lines) and experimental data for electrical power (denoted by red circles) and energy generation (represented by blue diamonds). Table 4 summarizes the obtained statistical indices for the discharging phase, focusing on the air reservoir system and the pressure regulator. As stated in Section 2.2.5, two models will be evaluated for the pressure regulator: the isenthalpic model and Cheayb et al.'s proposed model [27].

When observing the pressure regulator results for the two models, both show great accuracy in simulating the outlet temperature of the equipment. However, slightly better statistical indices are observed for the model proposed by Cheayl et al. [27], showing a MAPE of 0.21 %. This confirms that the model accurately simulates even beyond the validation range for pressures of 25–150 bar. Furthermore, the model exhibits remarkable accuracy with a maximum MAPE of 1.10 % for estimating the air reservoir system temperature.

Table 4
Statistical indices results for the discharging phase.

Parameters		RMSE	MAPE
Pressure regulator			
Temperature output, °C	Isenthalpic	1.17	0.39 %
	Cheayb et al.	0.98	0.21 %
Air reservoir system			
Temperature, °C		0.27	1.10 %
Pressure, bar		0.94	0.64 %
Air mass, kg		0.92	0.54 %

Finally, comparing the results to those reported in the literature provides additional confidence in the accuracy of the model. Chen et al. [25] validated their model by reporting a maximal MAPE of 8.0 %. With MAPE values consistently below 4.0 %, confidence in the model's capacity to accurately simulate the system's dynamics is engendered, thereby furnishing a robust groundwork for the subsequent parametric analyses.

3.3. Results of the parametric analysis

In the context of this study, the developed model facilitates the deliberate manipulation of parameters, aiming to systematically observe their impact on the system's RTE. Thus, this will help in proposing potential avenues for enhancements of aboveground CAES. The investigation encompasses variations in multiple parameters, including operational parameters such as ambient temperature and storage pressure, as well as design parameters such as polytropic indexes and stage configurations. As previously mentioned in Chapter 2 Materials and Methods, these parameter variations will be applied to two distinct system configurations: one without preheating before the expansion process and the other with reintroduced preheating before expansion. For these configurations, the analysis will focus on a single-stage expansion device represented by the last stage of the selected turbine (Table 9). Then, an examination of the outcomes associated with dividing the turbine into two and three stages will be conducted. It is noteworthy that this parametric analysis will entail modifying a single parameter at a time while holding the remaining parameters constant.

In addition to exploring parameter variations and their effects on the system's RTE, it is pertinent to establish a baseline RTE for the initial configuration of the aboveground CAES system. The initial configuration, characterized by a single-stage expansion device without preheating before the expansion process, presents inherent challenges to achieving high RTE. Through simulation, the RTE of this baseline configuration is determined to be 4.3 %, with a generated energy of 16.93 kWh and consumption of 366.75 kWh, utilizing maximum storage capacity with a storage pressure of 190 bar and a volume of 5.86 m3. These findings serve as a reference point for evaluating the impact of parameter modifications on system performance. Anticipated factors contributing to the low RTE include the absence of preheating, approximately 19 % mass loss in the compression chain, and relatively low efficiency of system components compared to those reported in existing literature. Moreover, the limitation of a single-stage expansion may further constrain RTE. If not explicitly analyzed, it will be assumed that the system operates at full capacity.

3.3.1. Effect of variation in the ambient temperature

The choice to examine ambient temperature as a key parameter in the analysis stems from its practical significance in real-world applications, such as integration with buildings or deployment in isolated areas, among other potential contexts. With seasonal changes and the potential for outdoor deployment of CAES units, understanding how ambient temperature fluctuations influence system performance is essential. This section investigates the impact of varying ambient temperatures on the operational dynamics of the CAES system, aiming to provide insights into its RTE across different climatic conditions.

Throughout this analysis, a constant ambient temperature is maintained across the operational cycle, ensuring consistency in the inlet air conditions for the compressor system and the surrounding environment. The ambient temperature discussed herein directly corresponds to external climate conditions. The analysis has been performed from −15 C to 25 °C and this parameter significantly influences the performance of the system during both charging and discharging phases, as illustrated in Fig. 11 and Fig. 12.

The variation in ambient temperature directly affects the initial stage of the compressor and the intercooling process between subsequent compressor stages, as the cooling air is drawn from the surrounding
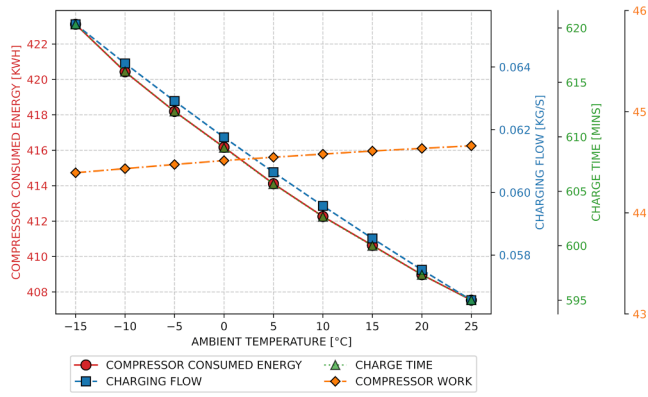
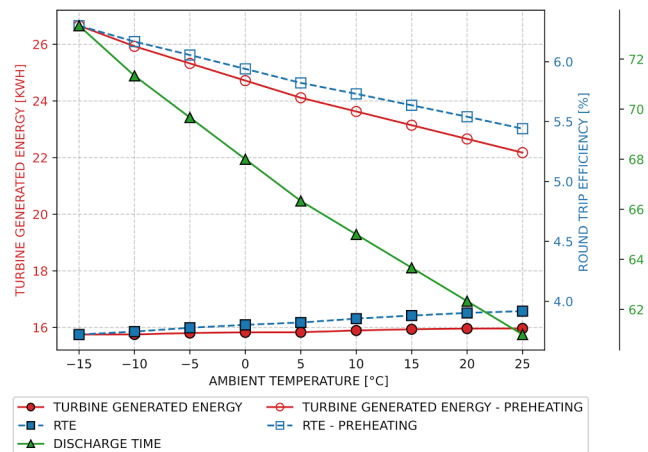**Fig. 11.** Effects of variation in the ambient temperature during the charge phase.

Fig. 12. Effects of variation in the ambient temperature during the discharge phase.

environment. Given that the compressor operates at a constant speed (1782 rpm), the volume flow (measured in m^3/s) entering the compressor also remains constant. However, the mass flow rate of the compressor (measured in kg/s) is influenced by the ambient temperature. This relation is illustrated in Fig. 11, showing a decrease in charging mass flow as ambient temperature rises, attributed to the reduction in air density. For instance, as the ambient temperature increases from −15 °C to 25 °C, the charging mass flow decreases from 0.065 kg/s to 0.056 kg/s. Additionally, with a constant volume reservoir, higher ambient temperatures result in higher pressure, allowing the system to reach maximum reservoir pressure more rapidly with charging time dropping to 595 min for a value of 25 °C, thereby shortening the charging phase. Consequently, due to this shorter charging process, the cumulative energy consumed by the compressor is reduced. Nonetheless, it is crucial to acknowledge that compressor workload slightly increases with rising temperature.

Upon analysis of the discharge phase depicted in Fig. 12, which includes results for both systems with and without preheating, an opposite trend is observed. In systems without preheating, a slight increase in turbine-generated energy is observed with rising ambient temperatures, despite a reduction of around 12 min in discharge time. Conversely, systems with preheating exhibit a decrease in turbine-generated energy, ranging from 27 kWh to 22 kWh, and a corresponding decline in RTE, ranging from 6.3 % to 5.4 %, with increasing ambient temperature. Drawing a parallel with climatic conditions, a colder climate presents natural advantages for CAES systems when expansion preheating is incorporated. Colder compression facilitates the storage of a larger mass

of air, while hotter expansion enables higher turbine-generated energy. Therefore, the interplay between compression and expansion temperatures is pivotal in optimizing system performance.

3.3.2. Effect of variating the storage maximum pressure

Increasing storage pressure offers a promising means to enhance stored energy without expanding storage volume. This strategy capitalizes on the principle that higher pressure rises energy density within a fixed volume. While advantageous for emergency backup systems focused on maximizing energy quantity stored, it may be different in scenarios characterized by daily charge and discharge cycles where maximizing the RTE is prioritized. Therefore, the goal is to determine whether it's better to fully fill the reservoir for daily charge and discharge cycles, like peak shaving or integration with intermittent renewables, or if it's more beneficial to fill it only as needed, considering demand prediction. To answer this, the effect of varying the maximum storage pressure of the air reservoir within the operational range of the equipment, spanning from 75 bar to 300 bar, will be examined.

During simulations of the charge phase, a notable trend emerged: as reservoir pressure increased, so did the workload on the compressor passing from 39 kWh to 48 kW at 300 bar. This observation suggests a potential adverse impact on the RTE as the stored air pressure increases. To address this hypothesis, the analysis in Fig. 13 explores the results of the discharge phases across maximum storage pressures.

The analysis of Fig. 13 elucidates the complex relationship between system efficiency and storage maximum pressure. While increasing storage pressure initially enhances RTE, a threshold appears at 150 bar for the preheated system and 125 bar for the non-preheated system. Beyond these thresholds, RTE declines: from 5.3 % to 5.1 % and from 4.2 % to 3.8 % for the preheated and non-preheated systems respectively. This phenomenon is attributed to increased losses due to higher compression work and heat generation at elevated pressures, ultimately diminishing overall system efficiency. Further investigation reveals that the working pressure of the turbine influences this threshold, wherein a higher-pressure turbine necessitates a higher reservoir maximum pressure to attain optimal efficiency. Operating system above the optimal pressure threshold risks inefficiencies and compromised performance, accentuating the importance of informed decision-making in CAES system design and operation.

In conclusion, the analysis highlights the possibility of optimizing storage maximum pressure in CAES systems, particularly in scenarios like peak shaving or intermittent renewables integration. While there exists an optimal storage maximum pressure, the findings suggest that it may not be necessary to completely fill the air storage, especially if the required energy can be accurately predicted. The results demonstrate
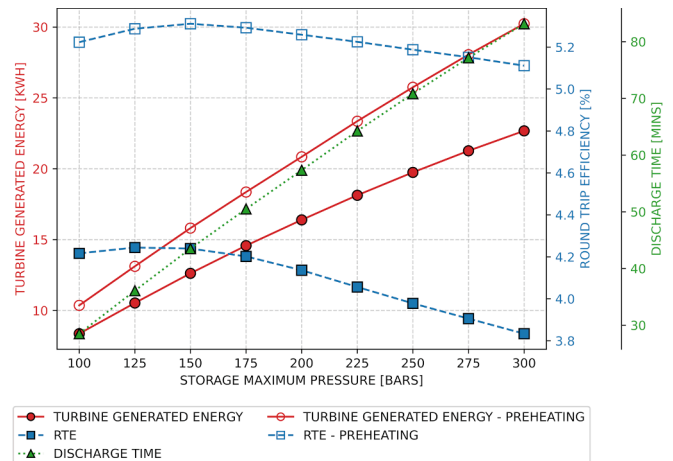

Fig. 13. Effects of variation in the storage maximum pressure during the discharge phase.

that an increase in storage pressure can lead to a decrease in RTE, underscoring the importance of careful consideration when designing and operating CAES systems.

3.3.3. Effects of variation in the polytropic index

This section focuses on understanding how variations in the polytropic index affect the system's performance. The scope or range of this numerical study is defined by the parameters investigated in other studies. For example, Patil et al. [44] demonstrated that utilizing liquid piston technology, such as injecting water spray, can lower the polytropic index from 1.27 to 1.06. This reduction led to a more efficient compression, aligning with the principles of I-CAES technology, where liquid piston technology is often employed to achieve near-isothermal compression. Fig. 14 and Fig. 15 illustrate the outcomes of adjusting the polytropic indexes of the compressor across the charging and discharging phases, respectively.

Here, achieving a near-isothermal process with a polytropic index close to 1 result in a significant reduction in compressor workload, with the workload dropping to less than 36 kW as depicted in Fig. 14. Despite the reduced workload, the near-isothermal transformations also lead to longer charging times, contributing to higher stored energy at a reduced energetic expense. This observation is in line with the fundamentals of the I-CAES approach, which underscores the importance of cooling air during compression to improve system efficiency while simultaneously storing recovered heat for subsequent utilization. By adopting such methods, CAES systems can effectively alleviate energy losses associated with conventional compression techniques.

Fig. 15 presents the discharge phase results for varied polytropic indices, both with and without preheating, highlighting the impact of near-isothermal conditions. Notably, near-isothermal conditions lead to an increase in turbine-generated work, albeit accompanied by a lengthened discharge time, ultimately resulting in a net increase in generated energy. For example, with a polytropic index of 1, turbine-generated energy reaches 17.9 kWh without preheating and escalates to 22.8 kWh with preheating. Additionally, combining near-isothermal processes with preheating before the expansion stage yields a RTE of 7.5 %.

3.3.4. Effect of variating the amount of expansion stages

In the endeavor to identify areas for improvement, a parameter analysis will be conducted focusing on the influence of multistage expansion on system performance. This decision was inspired by the findings of Chen et al. [25], who demonstrated a significant enhancement in the system's RTE through the integration of multiple expansion stages. The experiment will focus on analyzing the RTE for setups employing 1, 2, and 3 stages of expansion prior to the turbine parameters outlined in Table 9. It's important to note that the relevance of multistage expansion is contingent upon its conjunction with
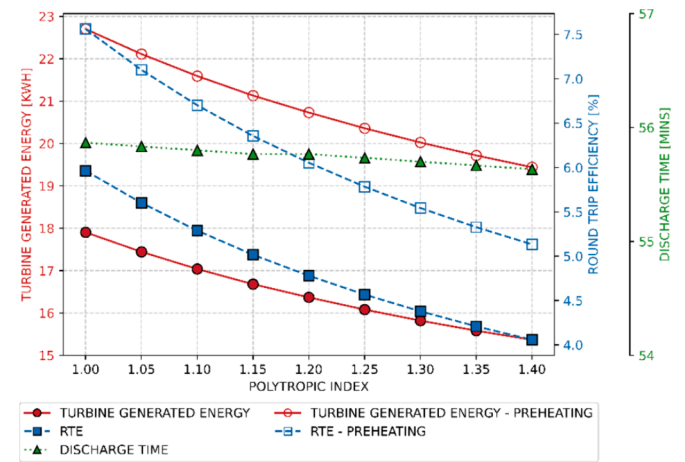
Fig. 15. Effects of variation in the polytropic index during the discharge phase.

preheating. Therefore, the evaluation will exclusively focus on scenarios where multistage expansion is combined with preheating.

The incorporation of multiple stages affects the system in some ways. Firstly, multistage expansion facilitates a greater combined expansion ratio, thereby augmenting power generation capabilities. Additionally, as the combined expansion ratio increases, so does the minimum working pressure. Consequently, when the compressed air reservoir pressure falls below the turbine's minimum working pressure, the discharge phase cannot operate properly, necessitating the cessation of the energy generation system. This leads to the accumulation of a dead mass of air within the system, adversely affecting both the charging and discharging phase duration.

Analyzing the charging results reveals that the compressor workload remains unaffected by the parameter variation. However, both the charging time and compressor consumed energy are impacted by the variation. With the rise in working pressure proportional to the amount of expansion stages, the charging consumed energy decreases from nearly 380 kWh to 290 kWh for 1–3 stages, indicating a considerable decrease in stored energy. To fully understand the effect on the RTE, Fig. 16 present simulation results for varying the expansion stages from 1 to 3.

In the discharge results presented in Fig. 16, although there are lower charge and discharge times indicating a reduced available stored energy quantity, the turbine-generated energy shows an increase as the amount of expansion stages rises for both systems. Consequently, there is a significant enhancement in RTE from 5.5 % to 16.0 % as the number of stages increases to 3. However, even if it appears that more stages will
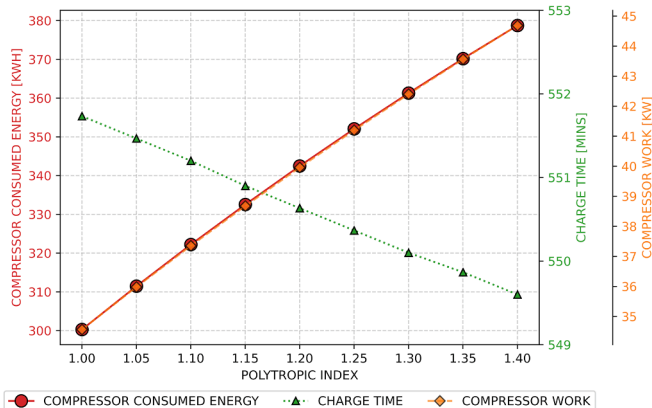
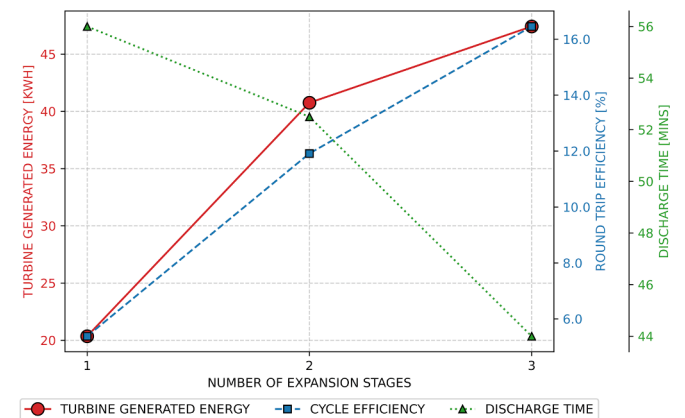**Fig. 14.** Effects of variation in the polytropic index during the charge phase.

Fig. 16. Effects of variation in the amount of expansion stages during the discharge phase.

result in a better RTE, the rate of improvement tends to diminish with the increase in the number of expansion stages, implying the feasibility of identifying an optimal stage count [25].

3.3.5. Potential of thermal energy storage system integration

The parametric analysis conducted previously has confirmed that preheating the air before the expansion process leads to an increase in generated energy and, consequently, enhances the system's RTE. Motivated by these findings and considering the compression ventilation needs, the feasibility of utilizing excess heat from the compressor to enhance the expansion system is now explored, while addressing the time delay between compression and expansion phases. A TES system such as the one shown in Fig. 17 must therefore be considered.

A TES system composed of dual tanks, as commonly used in solar power plants [45], is considered. During compression, the heat released is transferred to a thermal oil and stored in a hot tank. This stored energy is subsequently utilized by the triple-stage turbine as needed. The cooled thermal oil is then stored in a cold tank, ready to be reheated in the subsequent compression stage.

Given the critical role of temperature management within the system, two criteria should be met to confirm the feasibility of this TES system. First, the stored fluid temperature must be high enough to allow the compressed air to reach nominal turbine levels. Secondly, the quantity of stored thermal energy during the charging phase should be enough to account for the turbine preheating need. To validate these two criteria, the thermal requirement of the turbine will be determined and compared to the thermal release during compression. All these estimated energies are determined thanks to the developed model and considered a pressure maximum and minimum of respectively 190 and 55 bar representing the actual workbench limitations.

To assess the thermal demand for the triple-stage turbine, specific input parameters and model calculations are utilized. The input parameters include the mass flow and the outlet temperature for each stage of the turbine. The inlet temperature is determined by using the model, with the reservoir temperature for stage 1 and the turbine outlet temperature for stages 1 and 2 serving as inputs.

The required operating conditions for each stage of the turbine include outlet temperatures of 130 °C, 90 °C, and 90 °C for stages 1, 2, and 3, respectively. Utilizing the determined inlet and outlet temperatures, along with the mass flow rate of 0.321 kg/s, the heat transfer rate required for each stage to achieve the specified outlet temperatures are calculated using Eq. (7). The calculated heat transfer rates and total thermal energy demand are summarized in Table 5.

The calculated heat transfer rate necessary to elevate the temperature to the nominal state ranges from 33.5 kW to 38.0 kW for the first stage, 9.6 kW for the second stage, and 22.5 kW for the third stage. Integrating these values over the 40-min discharge period yields a total

**Table 5**
Energy demand analysis for triple-stage turbine.

Parameters	Stage 1	Stage 2	Stage 3
Heat transfer rate requirement, kW	33.5 – 38.0	9.6	22.5
Thermal energy transferred requirement, kWh	24.8	6.4	15.0
Total thermal transferred energy requirement, kWh	46.2		

thermal energy requirement of 46.2 kWh. Notably, the first stage exhibits a higher demand due to the maximum delta T reaching 115 °C during certain segments of the simulation.

While the total thermal energy requirement serves as a pertinent indicator of the turbine's operational requirements for achieving nominal performance, it is imperative to ensure that the heating fluid entering the heat exchanger maintains a temperature above 130 °C. The feasibility of achieving both the total thermal energy requirements extracted by the compressor system and the possibility of obtaining a fluid temperature of 130 °C will be discussed in the subsequent section.

The initial focus lies on carefully examining the inlet and outlet temperatures of the current compressor intercoolers. The transient data representing these temperatures are presented in Fig. 18.

Notably, the temperatures across the four stages exhibit significant elevation, with the three initial stages surpassing 150 °C and the third stage even exceeding 200 °C after 3 h of charging. This observation
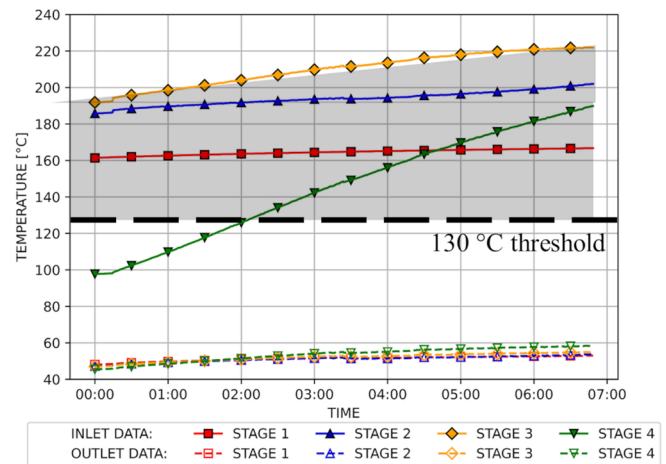
Fig. 18. Inlet and outlet temperatures for each stage of the heat exchangers during the charging phase.
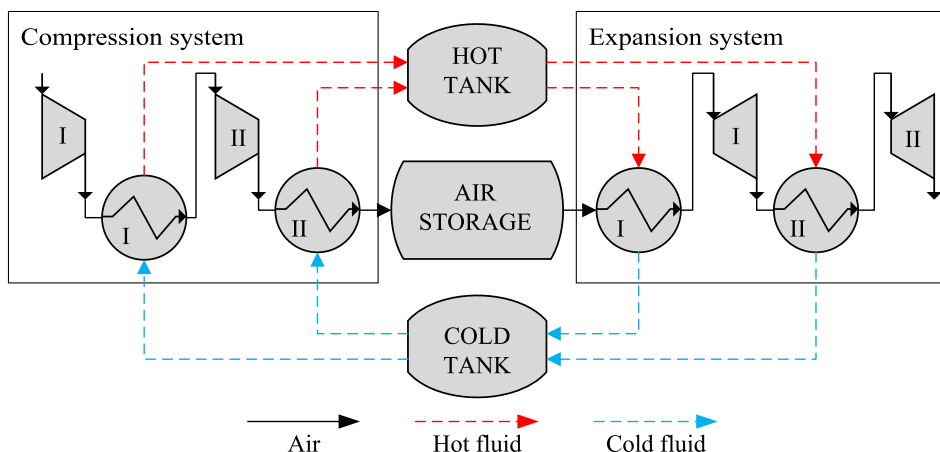
Fig. 17. Concept of an A-CAES using a hot and a cold tank for thermal storage.

suggests that the temperature of the compressed air is sufficiently high to elevate the thermal oil temperature above the required 130 °C threshold. However, this is only true if the associated energy level is also sufficient.

To determine if the available compression waste heat is sufficient, the focus will be solely on energy above 130 °C to maintain a conservative approach. Therefore, Eq. (7), will be revisited and adjusted accordingly. Input parameters for this calculation include the compressor's mass flow rate of 0.052 kg/s and an outlet temperature set at 130 °C. The results of this conservative analysis are summarized in Table 6.

Observing the results from Table 6, Stage 3 demonstrates the highest heat transfer rate, reaching 5.0 kW. Integrating the heat transfer rates over the 6.8-hour charging period, the waste heat for stages 1–4 amounts to 12.5 kWh, 23.4 kWh, 30.0 kWh, and 6.3 kWh, respectively. Consequently, the cumulative transferred thermal energy across all stages totals 72.2 kWh if only considering energy above 130 °C. It is worth noting that if all available waste energy is considered, a total of 189.2 kWh would be technically available. Comparing the available waste heat above 130 °C to the discharge total thermal energy transferred requirement (46.2 kWh), the value of 72.2 kWh greatly exceeds the requirement. Moreover, the combined waste heat from stages 2 and 3 could alone fulfill the thermal energy requirements.

In conclusion, the feasibility analysis demonstrates the substantial potential of storing extracted compression thermal energy in a TES system following the A-CAES concept. The waste heat extracted from the compression process, facilitated by the system's notably high compression temperatures, proves to be more than sufficient to compensate for preheating the selected triple-stage turbine if stored in a TES system. This highlights the feasibility and efficiency gains of utilizing the excess thermal energy for preheating purposes. Furthermore, even after fully reintroducing the required heat into the system before the expansion stages, a significant amount of waste heat remains unused. Specifically, if the whole waste heat was considered (189.2 kWh), 143 kWh of waste heat could potentially be harnessed to enhance turbine performance or for cogeneration purposes such as heating buildings or industrial processes. This presents a promising avenue for future research and development in the field of CAES.

4. Conclusion and recommendations

This study successfully validated the hypothesis that the development of a fully instrumented test bench and an advanced numerical model could significantly enhance the capability of representing the real behavior of small-scale aboveground CAES systems. The model, calibrated to reflect the experimental setup at Hydro-Québec's research institute, achieved a MAPE below 4.0 %, demonstrating its precision and reliability.

Confirming the second hypothesis, the parametric analysis provided valuable insights into potential system improvements, particularly regarding the preheating of air prior to the expansion stages. Specifically, preheating of the air before expansion stages. The analysis yielded several key insights:

- **Ambient Temperature:** Compressing air at lower temperatures reduces compressor workload and extends the charging duration, resulting in a 1.0 % increase in RTE.

- **Polytropic Index:** Reducing the polytropic index towards a near-isothermal process significantly enhances performance, achieving a 7.5 % increase in RTE with preheating.
- **Storage Pressures:** While higher storage pressures slightly reduce RTE, it remains significant when the objective is to maximize the amount of stored energy.
- **Expansion Stages:** Increasing the amount of expansion stages from one to three significantly improved RTE from 5.5 % to 16.0 %.

Based on the findings and analysis presented, several recommendations are proposed to further develop this project and advance the development and optimization of small-scale aboveground CAES systems:

- **Address the limitations of practical implementations**: future work could involve incorporating physical turbine components into the experimental setup, improving measurement techniques, and refining the model to account for additional real-world complexities. Enhanced computational resources and more comprehensive datasets could also facilitate more accurate and scalable implementations.
- **Address mass loss in air dryer**: Future work should focus on minimizing the substantial mass loss in the air dryer to enhance overall system efficiency.
- **Building and renewable integration**: Future work should aim at coupling the experimental workbench with a building or with a renewable source to collect data in real scenarios, providing practical insights into the system's performance in integrated environments.
- **Exergetic analysis**: Conduct a detailed exergetic analysis of each component within the CAES system to identify specific inefficiencies and guide strategic enhancements.
- **Thermal energy storage systems**: Further investigate and develop TES systems to efficiently store and utilize thermal energy from the compressor during discharge, thereby improving system efficiency through effective waste heat recovery.
- **Optimization of component sizing**: This study's parametric analysis sets the stage for a comprehensive optimization process that includes the sizing of components. Future research should explore the optimal sizing of compressors, expanders, and storage reservoirs to maximize system performance and efficiency.
- **Polytropic process improvements**: Efforts should be directed towards achieving near-isothermal compression and expansion processes to significantly enhance the RTE of CAES systems.

In conclusion, this research addresses key challenges in the development and optimization of small-scale aboveground CAES systems, which are vital for decentralized energy storage solutions. These systems offer a promising solution for balancing supply and demand, enhancing local grid stability, and integrating renewable energy sources. By improving the efficiency and reliability of small-scale CAES systems through advanced modeling and parametric analysis, this study contributes to the broader goal of achieving sustainable and resilient energy systems. The insights gained can inform the design and optimization of future small-scale CAES installations, making them more efficient, cost-effective, and practical for various applications. This research provides a robust framework for advancing the empirical and theoretical understanding of aboveground CAES systems, laying the groundwork for future advancements in CAES technology and contributing to the broader goal of enhancing energy storage solutions.

CRediT authorship contribution statement

Emeric Dormoy: Writing – original draft, Visualization, Validation, Methodology, Investigation, Formal analysis, Conceptualization. **Brice Le Lostec:** Writing – review & editing, Supervision, Methodology, Conceptualization. **Didier Haillot:** Writing – review & editing,

Table 6
Waste heat analysis for four stage compression (Above 130 °C).

Parameters	Stage 1	Stage 2	Stage 3	Stage 4
Heat transfer rate, kW	1.9	3.8	5.0	3.5
Waste heat, kWh	12.5	23.4	30.0	6.3
Total waste heat, kWh	72.2			

Validation, Supervision, Methodology, Funding acquisition, Conceptualization.

Declaration of competing interest

The authors declare the following financial interests/personal relationships which may be considered as potential competing interests: Emeric Dormoy reports financial support was provided by Mitacs Canada. If there are other authors, they declare that they have no known competing financial interests or personal relationships that could have appeared to influence the work reported in this paper.

Data availability

The authors do not have permission to share data.

Acknowledgments

Appendix A. Supplementary data

Supplementary data to this article can be found online at https://doi.org/10.1016/j.enconman.2024.119073.

References

[1] UNFCCC. Report of the Conference of the Parties serving as the meeting of the Parties to the Paris Agreement on its fifth session, held in the United Arab Emirates from 30 November to 13 December 2023. United Nations Framework Convention on Climate Change (UNFCCC), United Arab Emirates, FCCC/PA/CMA/2023/16/Add.1, Mar. 2024. [Online]. Available: https://unfccc.int/documents/637073.

[2] IEA. Greenhouse gas emissions from energy: overview. Int Energy Agency; 2021 [Online]. Available: https://www.iea.org/reports/greenhouse-gas-emissions-from-energy-overview.

[3] IEA. World energy outlook 2023. IEA, Paris, 2023. [Online]. Available: https://www.iea.org/reports/world-energy-outlook-2023.

[4] Budt M, Wolf D, Span R, Yan J. A review on compressed air energy storage: basic principles, past milestones and recent developments. Appl Energy 2016;170:250–68. https://doi.org/10.1016/j.apenergy.2016.02.108.

[5] Chen H, Cong TN, Yang W, Tan C, Li Y, Ding Y. Progress in electrical energy storage system: a critical review. Prog Nat Sci 2009;19(3):291–312. https://doi.org/10.1016/j.pnsc.2008.07.014.

[6] Aneke M, Wang M. Energy storage technologies and real life applications – a state of the art review. Appl Energy 2016;179:350–77. https://doi.org/10.1016/j.apenergy.2016.06.097.

[7] Luo X, Wang J, Dooner M, Clarke J. Overview of current development in electrical energy storage technologies and the application potential in power system operation. Appl Energy 2015;137:511–36. https://doi.org/10.1016/j.apenergy.2014.09.081.

[8] Zhang Z, et al. A review of technologies and applications on versatile energy storage systems. Renew Sustain Energy Rev 2021;148:111263. https://doi.org/10.1016/j.rser.2021.111263.

[9] Zakeri B, Syri S. Electrical energy storage systems: a comparative life cycle cost analysis. Renew Sustain Energy Rev 2015;42:569–96. https://doi.org/10.1016/j.rser.2014.10.011.

[10] Bazdar E, Sameti M, Nasiri F, Haghighat F. Compressed air energy storage in integrated energy systems: a review. Renew Sustain Energy Rev 2022;167:112701. https://doi.org/10.1016/j.rser.2022.112701.

[11] He W, Wang J. Optimal selection of air expansion machine in compressed air energy storage: a review. Renew Sustain Energy Rev 2018;87:77–95. https://doi.org/10.1016/j.rser.2018.01.013.

[12] Wang T, Yang C, Wang H, Ding S, Daemen JJK. Debrining prediction of a salt cavern used for compressed air energy storage. Energy 2018;147:464–76. https://doi.org/10.1016/j.energy.2018.01.071.

[13] Dooner M, Wang J. Compressed-air energy storage. In: Future energy. Elsevier; 2020. p. 279–312. https://doi.org/10.1016/B978-0-08-102886-5.00014-1.

[14] Chen L, Zheng T, Mei S, Xue X, Liu B, Lu Q. Review and prospect of compressed air energy storage system. J Mod Power Syst Clean Energy 2016;4(4):529–41. https://doi.org/10.1007/s40565-016-0240-5.

[15] Twitchell J. A review of state-level policies on electrical energy storage. Curr Sustain Renew Energy Rep 2019;6(2):35–41. https://doi.org/10.1007/s40518-019-00128-1.

[16] Wang J, et al. Overview of compressed air energy storage and technology development. Energies 2017;10(7):991. https://doi.org/10.3390/en10070991.

[17] Wolf D. *Methods for design and application of adiabatic compressed air energy: storage based on dynamic modeling.* In: UMSICHT-Schriftenreihe / Fraunhofer-Institut Umwelt-, Sicherheits-, Energietechnik UMSICHT, no. 65. Oberhausen: Laufen; 2011.

[18] APEX. Bethel Energy Center, APEX CAES. Accessed: Apr. 22, 2022. [Online]. Available: http://www.apexcaes.com/bethel-energy-center.

[19] Luo X, Wang J, Dooner M, Clarke J, Krupke C. Overview of current development in compressed air energy storage technology. Energy Proc 2014;62:603–11. https://doi.org/10.1016/j.egypro.2014.12.423.

[20] Wang J, Ma L, Lu K, Miao S, Wang D, Wang J. Current research and development trend of compressed air energy storage. Syst Sci Control Eng 2017;5(1):434–48. https://doi.org/10.1080/21642583.2017.1377645.

[21] Mei S, et al. Design and engineering implementation of non-supplementary fired compressed air energy storage system: TICC-500. Sci China Technol Sci 2015;58 (4):600–11. https://doi.org/10.1007/s11431-015-5789-0.

[22] Wilson I. Compressed air can compete and thrive in lithium age: Q&A. BloombergNEF. Accessed: May 02, 2022. [Online]. Available: https://about.bnef.com/blog/compressed-air-can-compete-and-thrive-in-lithium-age-qa/.

[23] Hydrostor. "Hydrostor," Site web de Hydrostor. [Online]. Available: https://www.hydrostor.ca/.

[24] SustainX. Technology performance report; 2015. [Online]. Available: https://www.smartgrid.gov/files/documents/Final-Technical-Report-SustainX_DE-OE0000231.pdf.

[25] Chen S, Arabkoohsar A, Zhu T, Nielsen MP. Development of a micro-compressed air energy storage system model based on experiments. Energy 2020;197:117152. https://doi.org/10.1016/j.energy.2020.117152.

[26] Dib G, Haberschill P, Rullière R, Perroit Q, Davies S, Revellin R. Thermodynamic simulation of a micro advanced adiabatic compressed air energy storage for building application. Appl Energy 2020;260:114248. https://doi.org/10.1016/j.apenergy.2019.114248.

[27] Cheayb M, Marin Gallego M, Tazerout M, Poncet S. Modelling and experimental validation of a small-scale trigenerative compressed air energy storage system. Appl Energy 2019;239:1371–84. https://doi.org/10.1016/j.apenergy.2019.01.222.

[28] Anderson K, Weritz J, Kaufman JG, editors. 6061 and Alclad 6061: general structural alloy. In: Properties and Selection of Aluminum Alloys, vol. 2B, ASM International; 2019. p. 0. doi:10.31399/asm.hb.v02b.a0006716.

[29] Ou KS, et al. Heat and mechanical response analysis of composite compressed natural gas cylinders at vehicle fire scenario. Proc Eng 2015;130:1425–40. https://doi.org/10.1016/j.proeng.2015.12.312.

[30] Khan MTI, Monde M. Characteristics of CFRP hydrogen storage vessel on rising temperature in the filling process. Proc Eng 2013;56:719–24. https://doi.org/10.1016/j.proeng.2013.03.184.

[31] Harris CR, et al. Array programming with NumPy. Nature 2020;585(7825):357–62. https://doi.org/10.1038/s41586-020-2649-2.

[32] Virtanen P, et al. SciPy 1.0: fundamental algorithms for scientific computing in Python. Nat Meth 2020;17(3):261–72. https://doi.org/10.1038/s41592-019-0686-2.

[33] McKinney W. Data structures for statistical computing in python. In: Presented at the Python in Science Conference, Austin, Texas, 2010, pp. 56–61. doi: https://doi.org/10.25080/Majora-92bf1922-00a.

[34] Hunter JD. Matplotlib: a 2D graphics environment. Comput Sci Eng 2007;9(3):90–5. https://doi.org/10.1109/MCSE.2007.55.

[35] Bell IH, Wronski J, Quoilin S, Lemort V. Pure and pseudo-pure fluid thermophysical property evaluation and the open-source thermophysical property library CoolProp. Ind Eng Chem Res 2014;53(6):2498–508. https://doi.org/10.1021/ie4033999.

[36] Çengel YA, Boles MA, Kanoglu M. Thermodynamics: an engineering approach. 9th ed. New York, NY: McGraw-Hill Education; 2019.

[37] Alami AH, et al. Experimental evaluation of compressed air energy storage as a potential replacement of electrochemical batteries. J Storage Mater 2022;54:105263. https://doi.org/10.1016/j.est.2022.105263.

[38] Lemmon EW, Jacobsen RT, Penoncello SG, Friend DG. Thermodynamic properties of air and mixtures of nitrogen, argon, and oxygen from 60 to 2000 K at pressures to 2000 MPa. J Phys Chem Ref Data 2000;29(3):331–85. https://doi.org/10.1063/1.1285884.

[39] Moran MJ, Shapiro HN. Fundamentals of engineering thermodynamics: SI version, SI units. 5th ed. Chichester: Wiley; 2006.

[40] Lallemand A. Compression et détente des gaz ou des vapeurs. Physique énergétique 2003. https://doi.org/10.51257/a-v1-be8013.

[41] Bergman TL, Lavine A, Incropera FP. Fundamentals of heat and mass transfer. Wiley abridged print companion. 8th ed. Hoboken, NJ: John Wiley & Sons Inc; 2019.

[42] Hoxton LG. The Joule-Thompson effect for air at moderate temperatures and pressures. Phys Rev 1919;13(6):438–79. https://doi.org/10.1103/PhysRev.13.438.

[43] Wang S, Zhang X, Yang L, Zhou Y, Wang J. Experimental study of compressed air energy storage system with thermal energy storage. Energy 2016;103:182–91. https://doi.org/10.1016/j.energy.2016.02.125.

[44] Patil VC, Acharya P, Ro PI. Experimental investigation of water spray injection in liquid piston for near-isothermal compression. Appl Energy 2020;259:114182. https://doi.org/10.1016/j.apenergy.2019.114182.

[45] Gil A, et al. State of the art on high temperature thermal energy storage for power generation. Part 1—Concepts, materials and modellization. Renew Sustain Energy Rev 2010;14(1):31–55. https://doi.org/10.1016/j.rser.2009.07.035.